

General bubble expansion at strong coupling

Jun-Chen Wang,^{1,*} Zi-Yan Yuwen,^{2,3,†} Yu-Shi Hao,^{2,3,‡} and Shao-Jiang Wang^{2,4,§}

¹*School of Physics, Peking University, Beijing 100871, China*

²*CAS Key Laboratory of Theoretical Physics, Institute of Theoretical Physics,
Chinese Academy of Sciences (CAS), Beijing 100190, China*

³*School of Physical Sciences, University of Chinese Academy of Sciences (UCAS), Beijing 100049, China*

⁴*Asia Pacific Center for Theoretical Physics (APCTP), Pohang 37673, Republic of Korea*

The strongly coupled system like the quark-hadron transition (if it is of first order) is becoming an active play yard for the physics of cosmological first-order phase transitions. However, the traditional field theoretic approach to strongly coupled first-order phase transitions is of great challenge, driving recent efforts from holographic dual theories with explicit numerical simulations. These holographic numerical simulations have revealed an intriguing linear correlation between the phase pressure difference (pressure difference away from the wall) to the nonrelativistic terminal velocity of an expanding planar wall, which has been reproduced analytically alongside both cylindrical and spherical walls from perfect-fluid hydrodynamics in our previous study but only for a bag equation of state. We also found, in our previous study, a universal quadratic correlation between the wall pressure difference (pressure difference near the bubble wall) to the nonrelativistic terminal wall velocity regardless of wall geometries. In this paper, we will generalize these analytic relations between the phase/wall pressure difference and terminal wall velocity into a more realistic equation of state beyond the simple bag model, providing the most general predictions so far for future tests from holographic numerical simulations of strongly coupled first-order phase transitions

I. INTRODUCTION

The cosmological first-order phase transition (FOPT) [1, 2] is a quantum field analog of quantum tunneling in quantum mechanics and thermal transition in statistical mechanics. For a quantum field theory that exhibits a continuous symmetry breaking with the appearance of a potential barrier [3], the cosmological FOPT occurs by randomly nucleating true-vacuum bubbles in the false-vacuum environment [4], and then proceeds by accelerating expansion of bubble walls [5, 6] driven by the potential difference that is eventually balanced by the backreaction force during the asymptotic expansion stage [7, 8], and finally ends by violent bubble wall collisions [9–12] with longstanding bulk fluid motions afterward [13–21]. The associated stochastic gravitational wave backgrounds (SGWBs) [22, 23] and curvature perturbations [24] or even the primordial black holes [25–30] provide comprehensive probes into our early Universe [31–33].

Although much attention on cosmological FOPTs has focused on the model buildings and parameter space searching at the electroweak scales (see, for example, [34] and references therein) for their apparent advantage of promising detection in space-borne GW detectors, the current observational data has already manifested the potential power in constraining the cosmological FOPT at corresponding energy scales of PT much higher or lower than the electroweak scales. For example, with the first

three observing runs of Advanced LIGO-Virgo’ data, the strong super-cooling FOPTs at LIGO-Virgo band have been marginally ruled out [35] when both contributions from wall collisions and sound waves are present as a general improvement to the previous works [36–39] with a single source. In particular, recent detection of SGWBs from the pulsar-timing-array (PTA) observations [40–43] has renewed the interest in strongly coupled system like the quark-gluon/hadron PT at the quantum chromodynamics (QCD) scales.

The cosmological PT of a strongly coupled system, if it is of first-order, has thus become an alternative probe in addition to the traditional heavy-ion collisions and lattice simulations for investigating the strong dynamics in QCD physics from various cosmological observations like the recent PTA constraints [44–62] at QCD scales. In particular, the PTA constraint [59] on the FOPT at QCD scales allows for the productions of solar-mass primordial black holes (PBHs) [25], which, however, might be disfavoured by the accompanying constraints from curvature perturbations [24] as shown specifically for a holographic QCD model [62]. On the other hand, the strongly coupled FOPT can in return serve as a play yard for exploring the nonequilibrium physics of cosmological FOPT. However, unlike the usual weakly coupled FOPT, the strongly coupled FOPT is difficult to deal with from the traditional perturbative field-theory approach due to its strong-dynamics nature.

Nevertheless, the holographic principle, especially the AdS/CFT correspondence [63–65] as a specific realization of the strong-weak duality, can be naturally applied to the strongly coupled FOPT in recent studies on bubble nucleation [66–72] and bubble expansion [73–76] as well as bubble-collision phenomenology [27, 62, 77–79]. In particular, the numerical simulations [73, 75] from two

* junchenwang@stu.pku.edu.cn

† yuwenziyan@itp.ac.cn (Corresponding author)

‡ haoyushi@itp.ac.cn

§ schwang@itp.ac.cn (Corresponding author)

very different holographic models reveal a similar linear correlation between the phase pressure difference¹ and the terminal velocity of an expanding planar wall as also derived analytically from a nonperturbative top-down approach [74]. However, such a correlation has not been explored yet in the holographic numerical simulation [76] for a cylindrical wall due to the high costs of computational power. Based on the same reason, the holographic numerical simulation has also not been conducted to date for the more realistic case of spherical wall expansion.

Intriguingly, besides the linear correlation between the phase pressure difference and terminal planar-wall velocity, the holographic numerical simulations [73, 75] have also unfolded two characteristic features for the strongly coupled FOPT: (i) The terminal wall velocity is marginally nonrelativistic. This can be understood that, as the bubble wall strongly interacts with the ambient plasma, the backreaction force is so rapidly growing that it only takes a very short time duration for the accelerating expansion stage until the backreaction force could balance the driving force. Hence, the strong dynamics can force the bubble wall to quickly saturate at a small velocity; (ii) The perfect-fluid hydrodynamics works extremely well in the whole range of bubble expansion except at the wall position. This can be understood as the bubble wall now moves so slowly (nonrelativistically) that the particles have enough time to fully thermalize before the bubble wall has swept over. Hence, the strong dynamics can also help to establish perfect-fluid hydrodynamic approximation except at the wall. Note that with appropriate junction conditions across the bubble wall, the perfect-fluid hydrodynamic approximation might as well work effectively at the wall position [7, 8].

The above-mentioned nonrelativistic terminal wall velocity and perfect-fluid hydrodynamics approximation revealed by the holographic numerical simulations for the strongly coupled FOPT have indicated that it might be feasible to derive the linear correlation between the phase pressure difference and terminal planar-wall velocity from bottom-up approach by fully appreciating the perfect-fluid hydrodynamics in the nonrelativistic limit of a planar-wall expansion. This is what we achieved in Ref. [80] not only for the planar wall but also for both cylindrical and spherical walls provided with a bag equation of state (EOS).

However, in both holographic numerical simulations and realistic models of strongly coupled FOPTs, the EOS cannot be fixed exactly by the bag model. It is therefore necessarily useful to generalize our previous study [80] directly into the case beyond the bag EOS, and in particular, to provide analytic approximations for practical

use without going over again the whole numerical evaluations. We therefore first set up the conventions and requisite formulas for later use in Sec. II, and then derive in the nonrelativistic wall limit for its correlations to the phase pressure difference and wall pressure difference in Sec. III and Sec. IV, respectively. Finally, the Sec. V is devoted to conclusions and discussions. Appendix A is provided for a self-containing introduction to the hydrodynamics beyond the bag EOS.

II. STRONGLY COUPLED FOPT

In this section, we will introduce the necessary notations and conventions closely following Ref. [8] in order to generalize the results of our previous study [80].

For a generally coupled system of scalar field and thermal plasma, the joined dynamics is governed by a series of Boltzmann equations for the distribution functions of each species. By considering the late stage of a fast FOPT, one can take advantage of simplifications from the flat-spacetime background, self-similar expansion, thin-wall geometry, and steady-state evolution. Therefore, the scalar-plasma system can be further reduced into a wall-fluid system [8] that can be well described by the perfect-fluid hydrodynamics with corresponding energy-momentum tensor of form

$$T^{\mu\nu} = (e + p)u^\mu u^\nu + p\eta^{\mu\nu}, \quad (1)$$

where e, p are the total energy density and pressure, and $u^\mu \equiv dx^\mu/d\tau$ is the four velocity of the fluid element at $x^\mu \equiv (t, z, x = 0, y = 0), (t, \rho, \varphi = 0, z = 0), (t, r, \theta = 0, \varphi = 0)$ for planar, cylindrical, and spherical wall geometries, respectively. Here, the corresponding coordinate systems are established at the center of the bubble in such a way that the fluid element only moves in the x^1 direction with the other two spatial directions fixed constantly, for example, all at zero. Hence, the four velocity of bulk fluids also reads $u^\mu = \gamma(v)(1, v, 0, 0)$ from the three velocity $v \equiv dx^1/dx^0$ via the Lorentz factor $\gamma(v) \equiv 1/\sqrt{1-v^2}$. The similarity of bubble expansion during the asymptotic stage at late time preferentially defines a convenient self-similar coordinate system ($T = t, X = x^1/x^0 \equiv \xi$) so that $v(\xi)$ traces the fluid velocity at $x^1 = \xi t$ in the background plasma frame. Besides, the steady-state expansion of the thin wall also preferentially defines an observer frame comoving with the wall at $x_w^1(x^0) = \xi_w t$ traced by the wall velocity ξ_w . Hence, in the comoving wall frame, the bulk-fluid four velocity reads $u^\mu = \bar{\gamma}(1, -\bar{v}, 0, 0)$ with $\bar{\gamma} \equiv \gamma(\bar{v}) = 1/\sqrt{1-\bar{v}^2}$, where the negative sign before the wall-frame three velocity $\bar{v} = (\xi_w - v)/(1 - \xi_w v) \equiv \mu(\xi_w, v)$ is introduced to ensure a positive \bar{v} for later convenience. Here, the abbreviation $\mu(\zeta, v(\xi)) \equiv (\zeta - v)/(1 - \zeta v)$ denotes for the Lorentz boost of the bulk fluid velocity $v(\xi)$ in the background plasma frame into a ζ -frame velocity seen in the comoving frame with velocity ζ .

¹ Note that, owing to the presence of sound shell with a nonvanishing fluid-velocity profile around the bubble wall, the phase pressure difference is different from the wall pressure difference, the former of which takes the pressure difference away from the bubble wall (in fact, away from the sound shell) while the latter of which takes the pressure difference near the bubble wall.

With the wall-fluid approximation for the coupled scalar-plasma system of cosmological FOPTs, the equation of motions (EoMs) of the wall-fluid system is given by the conservation of the total energy-momentum tensor $\nabla_\mu T^{\mu\nu} = 0$, which can be projected parallel along and perpendicular to the bulk fluid direction [81] that can be further combined into following equations for the profiles of fluid velocity $v(\xi)$ and total enthalpy $w(\xi) = e + p$,

$$D \frac{v}{\xi} = \gamma(v)^2 (1 - \xi v) \left(\frac{\mu(\xi, v)^2}{c_s^2} - 1 \right) \frac{dv}{d\xi}, \quad (2)$$

$$\frac{d \ln w}{d\xi} = \gamma(v)^2 \mu(\xi, v) \left(\frac{1}{c_s^2} + 1 \right) \frac{dv}{d\xi}. \quad (3)$$

Here $D = 0, 1, 2$ correspond to planar, cylindrical, and spherical walls [82], respectively, and the sound velocity $c_s = \sqrt{\partial_\xi p / \partial_\xi e}$ should be in general a function of ξ [83]. To further maintain the conservation of total energy-momentum tensor across the discontinuous interfaces at the bubble wall $\xi = \xi_w$ and shockwave front $\xi = \xi_{sh}$, appropriate junction conditions should be imposed from the temporal and spatial components of $\nabla_\mu T^{\mu\nu} = 0$. Specifically, in the comoving frame of the bubble wall, the following junction conditions,

$$w_- \bar{\gamma}_-^2 \bar{v}_- = w_+ \bar{\gamma}_+^2 \bar{v}_+, \quad (4)$$

$$w_- \bar{\gamma}_-^2 \bar{v}_-^2 + p_- = w_+ \bar{\gamma}_+^2 \bar{v}_+^2 + p_+, \quad (5)$$

are hold across the bubble wall, where w_\pm , p_\pm , \bar{v}_\pm , and $\bar{\gamma}_\pm \equiv \gamma(\bar{v}_\pm)$ are the enthalpy, pressure, wall-frame fluid velocity, and corresponding Lorentz factors just right in front and back of the bubble wall, respectively. Besides, in the comoving frame of the shockwave front, the following junction conditions,

$$w_L \tilde{\gamma}_L^2 \tilde{v}_L = w_R \tilde{\gamma}_R^2 \tilde{v}_R, \quad (6)$$

$$w_L \tilde{\gamma}_L^2 \tilde{v}_L^2 + p_L = w_R \tilde{\gamma}_R^2 \tilde{v}_R^2 + p_R, \quad (7)$$

are hold across the shockwave front, where $w_{R/L}$, $p_{R/L}$, $\tilde{v}_{R/L}$, and $\tilde{\gamma}_{R/L} \equiv \gamma(\tilde{v}_{R/L})$ are the enthalpy, pressure, shock-frame fluid velocity, and corresponding Lorentz factors just right in front and back of the shockwave front. Therefore, the combination of the fluid EoMs (2) and (3) with the junction conditions (4), (5), (6), and (7) together ensures the conservation of total energy-momentum tensor in the whole range of the fluid profile.

The fluid EoMs (2) and (3) can be readily solved numerically for the detonation and deflagration modes with the junction condition (4) at the bubble wall and junction condition (6) at the shockwave front (if any) provided with an extra assumption on the EOS. For a strongly coupled FOPT, the MIT bag EOS [84] is usually assumed as a good approximation with corresponding sound velocity $c_s = 1/\sqrt{3}$ independent of ξ . A more general EOS dubbed ν -model [85] renders two constant sound velocities $c_\pm^2 = \partial_\xi p_\pm / \partial_\xi e_\pm$ outside and inside of the bubble

wall, respectively, where

$$e_\pm = a_\pm T_\pm^{\nu_\pm} + V_0^\pm, \quad (8)$$

$$p_\pm = c_\pm^2 a_\pm T_\pm^{\nu_\pm} - V_0^\pm \quad (9)$$

are the total energy density and pressure just right in the front and back of the bubble wall, respectively. Here, $V_0^\pm \equiv V_0(\phi_\pm)$ is the zero-temperature part of total effective potential $V_{\text{eff}}(\phi, T) = V_0(\phi) + \Delta V_T(\phi, T)$ at the false and true vacua ϕ_\pm , respectively. It is easy to see that $\nu_\pm = 1 + 1/c_\pm^2$. With above ν -model EOS, the wall-frame fluid velocities \bar{v}_\pm from the junction conditions (4) and (5) can be related by

$$\bar{v}_+ = \frac{1}{1 + \alpha_+} \left(q X_+ \pm \sqrt{q^2 X_-^2 + \alpha_+^2 + (1 - c_+^2) \alpha_+ + q^2 c_-^2 - c_+^2} \right), \quad (10)$$

with abbreviations $q \equiv (1 + c_+^2)/(1 + c_-^2)$, $X_\pm \equiv \bar{v}_-/2 \pm c_-^2/(2\bar{v}_-)$, $\alpha_+ \equiv \Delta V_0/(a_+ T_+^{\nu_+})$, and $\Delta V_0 \equiv V_0^+ - V_0^-$. One can also define the strength factor $\alpha_N \equiv \Delta V_0/(a_+ T_N^{\nu_+})$ at null infinity $\xi = 1$ (unperturbed by fluid motions) so that $\alpha_+ w_+ = \alpha_N w_N = (1 + c_+^2) \Delta V_0$. The hydrodynamic solutions for the above ν -model EOS can be solved numerically in Appendix A.

To see the nonrelativistic behavior of the phase pressure difference (driving force per unit area) between the innermost and outermost parts of the fluid profile [7, 8],

$$\begin{aligned} p_{\text{dr}} &= \Delta V_{\text{eff}} = -\Delta p = \Delta(-c_s^2 a T^\nu + V_0) \\ &= -\frac{c_+^2}{1 + c_+^2} w_N + \frac{c_-^2}{1 + c_-^2} w_O + \frac{1}{1 + c_+^2} \alpha_N w_N, \end{aligned} \quad (11)$$

we consider the deflagration expansion of bulk fluid with a compressive shockwave as a sound shell in front of the bubble wall, in which case we can equal the enthalpy at null infinity $w_N \equiv w(\xi = 1) = w(\xi = \xi_{sh} + 0^+) \equiv w_R$ to the enthalpy just in front of the shockwave front, and equal the enthalpy at the origin $w_O \equiv w(\xi = 0) = w(\xi = \xi_w + 0^-) \equiv w_-$ to the enthalpy just behind the bubble wall. Further note that w_- can be even reduced to depend only on ξ_w , v_+ , and w_+ by adopting the junction condition (4) with $\bar{v}_+ = \mu(\xi_w, v_+)$ and $\bar{v}_- = \xi_w$, where w_+ can be further expressed in terms of ξ_w , v_+ , and observable parameters at null infinity like α_N and ω_N by

$$w_+ = \frac{(1 + c_-^2)(1 - v_+^2) \xi_w \alpha_N w_N}{c_+^2 (\xi_w + c_-^2 v_+) (1 - v_+ \xi_w) - (c_-^2 + v_+ \xi_w) (\xi_w - v_+)} \quad (12)$$

from the minus-sign branch of (10). Now the phase pressure difference reads purely in terms of the sound velocities c_\pm , null-infinity observables α_N and w_N , bubble wall velocity ξ_w , and fluid velocity v_+ (to be determined

later),

$$\frac{p_{\text{dr}}}{w_N} = \left[\frac{1}{1 + c_+^2} + \frac{c_-^2(\xi_w - v_+)(1 - v_+\xi_w)}{c_+^2(\xi_w + c_-^2 v_+)(1 - v_+\xi_w) - (c_-^2 + v_+\xi_w)(\xi_w - v_+)} \right] \alpha_N - \frac{c_+^2}{1 + c_+^2}, \quad (13)$$

where $v_+ = \mu(\xi_w, \bar{v}_+(\xi_w, \alpha_+))$ from the minus-sign branch of (10) can be further reduced in terms of ξ_w and α_+ . Therefore, as long as we can find a relation between α_+ and α_N , which can be achieved approximately to the leading order (LO) in ξ_w for planar, cylindrical, and spherical walls, we can eventually arrive at the direct relation between the phase pressure difference p_{dr} and bubble wall velocity ξ_w solely in terms of the ν -model EOS c_{\pm} and null-infinity observables α_N and w_N without reference to the underlying microscopic physics.

III. PHASE PRESSURE DIFFERENCE

In this section, we analytically derive the approximated relation between the phase pressure difference $p_{\text{dr}} = \Delta V_{\text{eff}} = p_O - p_N$ and the bubble wall velocity ξ_w with ν -model EOS for planar, cylindrical, and spherical wall geometries.

A. Planar wall

For a planar wall, the nonvanishing fluid profile is depicted by the fluid EoM (2) with $D = 1$,

$$(\mu(\xi, v)^2 - c_+^2) \frac{dv}{d\xi} = 0, \quad (14)$$

whose solutions are either $dv/d\xi = 0$, namely, $v = \text{const.}$, or $\mu(\xi, v) = c_+$, which would lead to $\xi > c_+$ for $v > 0$ but with no deflagration regime. Hence, the only solution should be $v = \text{const.} = v_+$ in the sound shell and the corresponding enthalpy profile from (3) with $dv/d\xi = 0$ also stays constant in the sound shell, $w_+ = \text{const.} = w_L$. This w_L can be related to $w_R = w_N$ by the junction condition (6) via $\tilde{v}_R = \xi_{sh}$ and $\tilde{v}_L = \mu(\xi_{sh}, v_{sh})$ from the fluid velocity $v_{sh} \equiv v(\xi_{sh} + 0^-)$ just behind the shockwave front ξ_{sh} . To further determine v_{sh} and ξ_{sh} , note that the constant velocity profile in the sound shell implies $v_{sh} = v_+ = \mu(\xi_w, \bar{v}_+(\bar{v}_-, \alpha_+))$ with $\bar{v}_- = \xi_w$ and $\bar{v}_+(\bar{v}_-, \alpha_+)$ given by the minus-sign branch of (10). Thus, v_{sh} can be expressed in terms of ξ_w and α_+ alone. Once v_{sh} is determined, ξ_{sh} can be directly obtained from the shock front condition $\mu(\xi_{sh}, v_{sh})\xi_{sh} = c_+^2$. Hence, $\alpha_N/\alpha_+ = w_+/w_N$ can be derived in terms of ξ_w and α_+ alone,

which can be expanded as

$$\frac{\alpha_N}{\alpha_+} = 1 + \frac{c_-^2 - c_+^2 + (1 + c_-^2)\alpha_+}{c_-^2 c_+} \xi_w + \frac{[c_-^2 - c_+^2 + (1 + c_-^2)\alpha_+]^2}{2c_-^4 c_+^2} \xi_w^2 + \mathcal{O}(\xi_w^3). \quad (15)$$

We can reverse the above relation to get α_+ expressed in terms of ξ_w and α_N . Then, we can plug $\alpha_+(\xi_w, \alpha_N)$ into the minus-sign branch of (10) to get $\bar{v}_+(\bar{v}_- \equiv \xi_w, \alpha_+(\xi_w, \alpha_N))$. Next, we can further expand $v_+ = \mu(\xi_w, \bar{v}_+(\xi_w, \alpha_N))$ in ξ_w , which finally yields the phase pressure difference (13) in the small ξ_w limit up to the next-to-leading order (NLO) as

$$\frac{p_{\text{dr}}}{w_N} = \frac{c_+[c_-^2 - c_+^2 + (1 + c_-^2)\alpha_N]}{c_-^2(1 + c_+^2)} \xi_w + \frac{c_-^2 - c_+^2 + (1 + c_-^2)\alpha_N}{2c_-^4(1 + c_+^2)^2} [\alpha_N - c_+^4 - c_+^2(3 + \alpha_N) + c_-^2(1 - c_+^2)(1 + \alpha_N)] \xi_w^2 + \mathcal{O}(\xi_w^3). \quad (16)$$

In the bag limit $c_{\pm} = c_s$, this analytic approximation reduces to the same linear correlation $p_{\text{dr}} = \alpha_N w_N \xi_w / c_s + \mathcal{O}(\xi_w^2)$ at the leading order as our previous estimation [80]. To see the goodness of fit for our analytical approximation, we can separately evaluate the phase pressure difference numerically from the exact numerical solutions, and then find a perfect match for both cases with $c_+ > c_-$ and $c_+ < c_-$ at NLO as shown in Fig. 1. This leading-order linear dependence in the planar-wall velocity can be tested explicitly in Sec. V with respect to the holographic numerical simulation of a strongly coupled FOPT with a planar wall [73].

B. Cylindrical wall

For a cylindrical wall with $D = 1$, the fluid EoM (2) to the order of v^2 ,

$$\frac{dv}{d\xi} = \frac{c_+^2 v}{\xi(\xi^2 - c_+^2)} - \frac{(c_+^2 + \xi^2 - 2)c_+^2 v^2}{(c_+^2 - \xi^2)^2} + \mathcal{O}(v^3), \quad (17)$$

can be solved as

$$v(\xi) = \frac{c_+(c_+^2 - \xi^2)}{\xi} \Big/ \left[2c_+(c_+^2 - 1) + \frac{1}{v_+\xi_w} \sqrt{\frac{c_+^2 - \xi^2}{c_+^2 - \xi_w^2}} \text{Sol} \right], \quad (18)$$

$$\text{Sol} = c_+\xi_w(2v_+ - \xi_w) + c_+^3(1 - 2v_+\xi_w)$$

$$+ v_+\xi_w(c_+^2 - 2)\sqrt{c_+^2 - \xi_w^2} \ln \left(\frac{\xi \left(c_+ + \sqrt{c_+^2 - \xi_w^2} \right)}{\xi_w \left(c_+ + \sqrt{c_+^2 - \xi^2} \right)} \right)$$

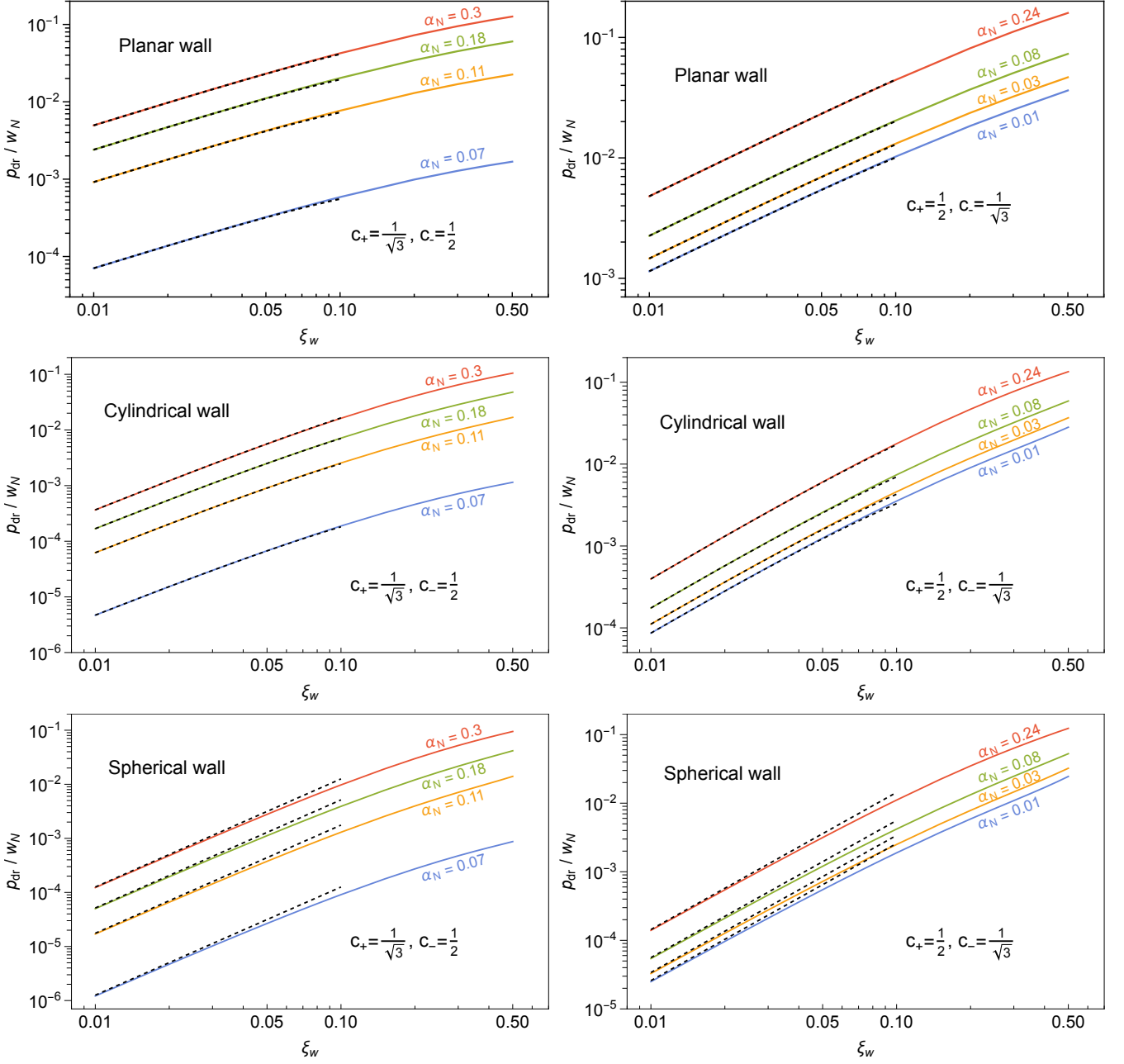


FIG. 1. The comparison between our analytical approximations (dashed lines) and the exact numerical evaluations (solid lines) for the relations (16) (top), (20) (middle), and (24) (bottom) between the phase pressure difference p_{dr}/w_N and wall velocity ξ_w given some illustrative values for the asymptotic strength factor α_N in both cases of ν -model EOS with sound velocities $c_+ > c_-$ (left) and $c_+ < c_-$ (right).

given the condition $v(\xi_w + 0^+) = v_+$ at the bubble wall. It is easy to see from (18) that the shock front where $v(\xi)$ drops to zero is now approximated at $\xi = \xi_{sh} = c_+$ with $w(c_+) = w_N$, from which we can integrate the fluid EoM (3) to evaluate w_+ at ξ_w from $d \ln w/d\xi$ as estimated shortly below. To estimate $d \ln w/d\xi$, we first insert (18) into (3) and then expand $d \ln w/d\xi$ to the order of v_+^2 . Hence, $\alpha_N/\alpha_+ = w_+/w_N$ is now a function of ξ_w , α_+ , and $v_+ = \mu(\xi_w, \bar{v}_+)$. After inserting $\bar{v}_+(\xi_w, \alpha_+)$ from the

minus-sign branch of (10), α_N/α_+ can be expanded in the small ξ_w limit as

$$\frac{\alpha_N}{\alpha_+} = 1 + \frac{c_-^2 - c_+^2 + (1 + c_-^2)\alpha_+}{2c_-^4 c_+^2 (1 + c_+^2)} \left[c_+^2 - c_-^2 - (1 + c_-^2)\alpha_+ + 2c_-^2 (1 + c_+^2) \ln \frac{2c_+}{\xi_w} \right] \xi_w^2 + \mathcal{O}(\xi_w^4). \quad (19)$$

Reversing the above relation to get $\alpha_+(\xi_w, \alpha_N)$ and plugging it into the minus-sign branch of (10), we can derive $\bar{v}_+(\xi_w, \alpha_N)$ as a function of ξ_w and α_N . We next further expand $v_+ = \mu(\xi_w, \bar{v}_+(\xi_w, \alpha_N))$ in terms of ξ_w and then insert it into (13), finally the phase pressure difference can be obtained in the small ξ_w limit as

$$\frac{p_{\text{dr}}}{w_N} = \frac{c_-^2 - c_+^2 + (1 + c_-^2)\alpha_N}{2c_-^4(1 + c_+^2)^2} [(1 + c_-^2)\alpha_N - (c_+^2 + 2c_+^2c_-^2 + c_-^2) + 2c_-^2(1 + c_+^2) \ln \frac{2c_+}{\xi_w}] \xi_w^2 + \mathcal{O}(\xi_w^4). \quad (20)$$

Note that the purely quadratic term in ξ_w in the above approximation is actually an NLO term, while the term proportional to $\xi_w^2 \ln \xi_w$ is at the leading order as it is larger than the purely quadratic term in ξ_w . This analytic expression serves as an even better approximation in the bag limit $c_{\pm} \rightarrow c_s = 1/\sqrt{3}$ compared to our previous estimation [80], and also perfectly matches the exact numerical evaluation as shown in Fig. 1 for both cases with $c_+ > c_-$ and $c_+ < c_-$, where the distinctive logarithmic dependence can be directly tested in future holographic numerical simulations of strongly coupled FOPTs with a cylindrical wall [76].

C. Spherical wall

For a spherical wall with $D = 2$, the fluid EoM (2) to the order of v^2 ,

$$\frac{dv}{d\xi} = \frac{2c_+^2 v}{\xi(\xi^2 - c_+^2)} - \frac{2(c_+^2 + \xi^2 - 2)c_+^2 v^2}{(c_+^2 - \xi^2)^2} + \mathcal{O}(v^3), \quad (21)$$

can be solved as

$$v(\xi) = \frac{c_+ v_+ \xi_w^2 (c_+^2 - \xi^2)}{\xi} \Big/ [c_+^3 \xi + 2c_+ v_+ \xi_w (c_+^2 - 2)\xi - c_+ \xi_w^2 (2c_+^2 v_+ - 4v_+ + \xi) + \text{Sol}] \quad (22)$$

$$\text{Sol} = 4v_+ \xi_w^2 (c_+^2 - 1) \left[\text{arctanh} \left(\frac{\xi}{c_+} \right) - \text{arctanh} \left(\frac{\xi_w}{c_+} \right) \right] \xi$$

given the condition $v(\xi_w + 0^+) = v_+$ at the bubble wall. Following the same procedures as in the cylindrical case, we can obtain estimate $d \ln w / d\xi$ by first plugging (22) into (3) and then expanding it to the order of v_+^2 . Hence, $\alpha_N / \alpha_+ = w_+ / w_N$ is obtained by integrating $d \ln w / d\xi$. After inserting $v_+ = \mu(\xi_w, \bar{v}_+(\xi_w, \alpha_+))$, α_N / α_+ as a function of ξ_w and α_+ can be expanded in the small ξ_w limit as

$$\frac{\alpha_N}{\alpha_+} = 1 + \frac{c_-^2 - c_+^2 + (1 + c_-^2)\alpha_+}{2c_-^4 c_+^2 (1 + c_+^2)} [c_+^2 + 3c_-^2 + 4c_+^2 c_-^2 - (1 + c_-^2)\alpha_+] \xi_w^2 + \mathcal{O}(\xi_w^3). \quad (23)$$

Reversing the above relation to obtain $\alpha_+(\xi_w, \alpha_N)$ and substituting it into the minus-sign branch of (10), we can derive $\bar{v}_+(\xi_w, \alpha_N)$ as a function of ξ_w and α_N . We next further expand $v_+ = \mu(\xi_w, \bar{v}_+(\xi_w, \alpha_N))$ in terms of ξ_w and then substitute it into (13), finally the phase pressure difference can be obtained in the small ξ_w limit as

$$\frac{p_{\text{dr}}}{w_N} = \frac{c_-^2 - c_+^2 + (1 + c_-^2)\alpha_N}{2c_-^4(1 + c_+^2)^2} [3c_-^2 - c_+^2 + 2c_+^2 c_-^2 + (1 + c_-^2)\alpha_N] \xi_w^2 + \mathcal{O}(\xi_w^4). \quad (24)$$

This analytical expression serves as an even better approximation in the bag limit $c_{\pm} \rightarrow c_s = 1/\sqrt{3}$ compared to our previous estimation [80], and also perfectly matches the exact numerical evaluation as shown in Fig. 1 for both cases with c_+ and c_- although the matching is not as good as the planar and cylindrical cases as here we only include the leading-order quadratic term while the NLO quartic term is too lengthy to be informative. This leading-order pure quadratic dependence in the spherical wall velocity can be directly tested in future holographic numerical simulations of strongly coupled FOPTs with a spherical wall.

IV. WALL PRESSURE DIFFERENCE

Apart from the phase pressure difference away from the bubble wall, we can also approximate in the nonrelativistic limit for the pressure difference near the bubble wall, $\Delta_{\text{wall}} p \equiv p_+ - p_-$, which can be evaluated by the junction condition (5),

$$\frac{\Delta_{\text{wall}} p}{w_N} = \frac{\bar{\gamma}_-^2 \bar{v}_-^2 w_- - \bar{\gamma}_+^2 \bar{v}_+^2 w_+}{w_N}. \quad (25)$$

For the deflagration mode with $\bar{v}_- = \xi_w$ and $\bar{v}_+ = \mu(\xi_w, v_+)$, we can solve α_+ from the minus-branch of (10) as

$$\alpha_+ = \frac{1}{(c_-^2 + 1)(v_+^2 - 1)\xi_w} [v_+ \xi_w (\xi_w - v_+) + c_+^2 \xi_w (v_+ \xi_w - 1) + c_-^2 (\xi_w - v_+ - v_+ c_+^2 + v_+^2 c_+^2 \xi_w)]. \quad (26)$$

Combining (25) and (26), we can obtain the wall pressure difference $\Delta_{\text{wall}} p / w_N$ in terms of c_{\pm} , ξ_w , α_N , and v_+ as

$$\frac{\Delta_{\text{wall}} p}{w_N} = \frac{[(1 + c_-^2)(v_+ - \xi_w)\xi_w v_+ \alpha_N]}{w_N} \Big/ \{ \xi_w v_+ (\xi_w - v_+) + c_+^2 \xi_w (\xi_w v_+ - 1) + c_-^2 [\xi_w + v_+ (c_+^2 \xi_w v_+ - c_+^2 - 1)] \}, \quad (27)$$

where we have converted w_- to w_+ via the junction condition (4), and then converted w_+ to w_N via $w_+ \alpha_+ = w_N \alpha_N$. After plugging the nonrelativistic analytic approximations $v_+(\xi_w, \alpha_N)$ we obtained in the previous three subsections for planar, cylindrical, and spherical

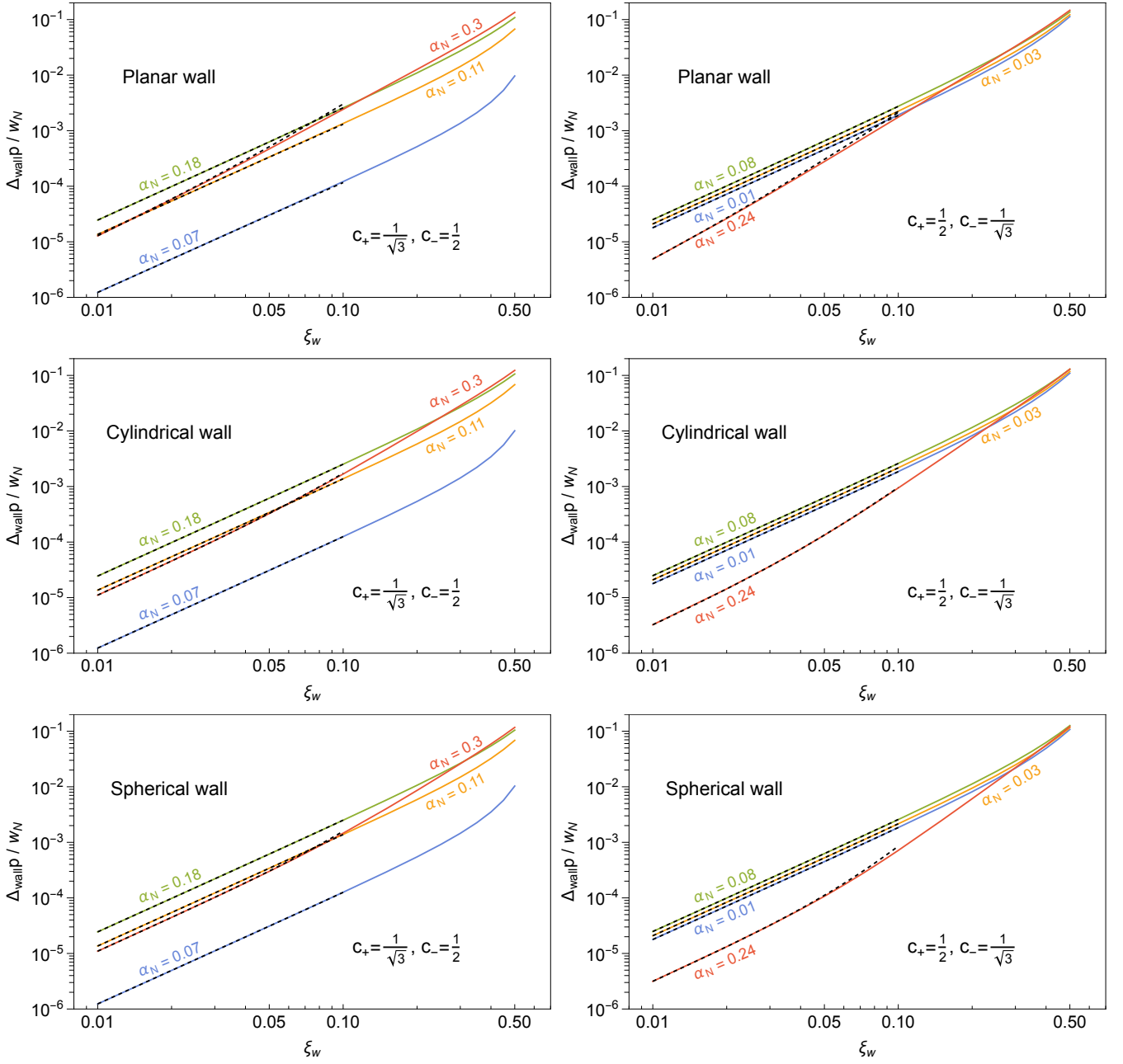


FIG. 2. The comparison between our analytical approximation (28) (dashed lines) [with additional next-to-leading order correction (30) for relatively large $\alpha_N = 0.24, 0.3$] and the exact numerical evaluations (solid lines) for the relation between the wall pressure difference p/w_N and terminal velocity ξ_w (solid lines) of planar (top), cylindrical (middle), and spherical (bottom) walls, respectively, given some illustrative values for the asymptotic strength factor α_N in both cases with sound velocities $c_+ > c_-$ (left) and $c_+ < c_-$ (right).

walls into (27), we finally arrive at a universal quadratic dependence in the wall velocity at the leading order for the wall pressure difference in the small ξ_w limit as

$$\left(\frac{\Delta_{\text{wall}} p}{w_N}\right)_{\text{LO}}^{D=0,1,2} = \frac{(1+c_-^2)(c_+^2 - \alpha_N)[c_-^2 - c_+^2 + \alpha_N(1+c_-^2)]}{c_-^4(1+c_+^2)^2} \xi_w^2, \quad \left(\frac{p_+ - p_-}{w_N}\right)_{\text{LO}, c_{\pm} \rightarrow c_s}^{D=0,1,2} = \left(\frac{\alpha_N}{c_s^2} - \frac{\alpha_N^2}{c_s^4}\right) \xi_w^2. \quad (28)$$

whose bag limit $c_{\pm} \rightarrow c_s$ is the same as our previous result [80],

This universal scaling for different wall shapes can be understood as the pressure difference taken near the wall

does not care about its global shape. This is different from the phase pressure difference taken between the null infinity and bubble center, which does care about the global shapes of the bubble wall, containing not only the information near the bubble wall but also the whole bubble-fluid system including the sound shell and shock-wave front (if any). This is why the phase pressure differ-

ence admits different leading-order behaviors, that is, the leading-order linear, logarithmic-quadratic, and purely quadratic dependences for the planar, cylindrical, and spherical walls, respectively. Nevertheless, for the asymptotic strength factor α_N taking a relatively large value, the leading-order analytical approximation is not enough, and we must consider the next leading-order correction,

$$\begin{aligned} \left(\frac{p_+ - p_-}{w_N}\right)_{\text{NLO}}^{D=0} &= \frac{(1 + c_-^2)[c_-^2 - c_+^2 + \alpha_N(1 + c_-^2)][c_+^2 c_-^2 - c_+^4 + \alpha_N^2(1 + c_-^2)]}{c_-^6 c_+ (1 + c_+^2)^2} \xi_w^3, \\ \left(\frac{p_+ - p_-}{w_N}\right)_{\text{NLO}}^{D=1} &= \frac{(1 + c_-^2)[c_-^2 - c_+^2 + \alpha_N(1 + c_-^2)]}{2c_-^8 c_+^2 (1 + c_+^2)^4} (\text{Cy}_1 + \text{Cy}_2 + \text{Cy}_3 + \text{Cy}_4) \xi_w^4, \\ \left(\frac{p_+ - p_-}{w_N}\right)_{\text{NLO}}^{D=2} &= \frac{(1 + c_-^2)[c_-^2 - c_+^2 + \alpha_N(1 + c_-^2)]}{2c_-^8 c_+^2 (1 + c_+^2)^4} (\text{Sp}_1 + \text{Sp}_2 + \text{Sp}_3) \xi_w^4, \end{aligned} \quad (30)$$

with

$$\begin{aligned} \text{Cy}_1 &= (c_+^2 - \alpha_N)^2 (c_+^4 + 3c_+^2 + c_+^2 \alpha_N - \alpha_N) + (4 \ln 2) c_-^2 c_+^2 \alpha_N^2 + c_-^2 \alpha_N (c_+^2 - \alpha_N) (1 + 2\alpha_N - 2 \ln 2), \\ \text{Cy}_2 &= -c_-^2 (c_+^2 - \alpha_N) [(2 \ln 2) c_+^6 - c_+^4 [4 + 3\alpha_N - (2 \ln 2) \alpha_N] + c_+^2 (2\alpha_N^2 + 4\alpha_N + 2 \ln 2)], \\ \text{Cy}_3 &= c_-^4 \left[c_+^6 (2 + 2 \ln 2 + 2\alpha_N) + c_+^4 [(2 \ln 2 - 4) \alpha_N^2 - 5\alpha_N - 1 + 4 \ln 2] + \text{Cy}'_3 \right], \\ \text{Cy}'_3 &= c_+^2 [\alpha_N^3 + (4 \ln 2 + 1) \alpha_N^2 - \alpha_N + 2 \ln 2 - 1] - \alpha_N^2 (1 - 2 \ln 2 + \alpha_N) \\ \text{Cy}_4 &= 2c_-^2 \left[(\alpha_N^2 (1 + c_+^2)^2 + c_-^2 (1 + c_+^2)^2 (c_+^2 + \alpha_N^2) - (1 + c_+^4) c_+^4) \ln \left(\frac{c_+}{\xi_w} \right) - 2c_+^6 \ln \left(\frac{2c_+}{\xi_w} \right) \right] \\ \text{Sp}_1 &= (c_+^2 - \alpha_N)^2 (c_+^4 + 3c_+^2 + c_+^2 \alpha_N - \alpha_N), \\ \text{Sp}_2 &= -c_-^2 (c_+^2 - \alpha_N) [4c_+^6 + c_+^4 (4 + \alpha_N) + 2c_+^2 (\alpha_N^2 + 6\alpha_N + 2) + \alpha_N (3 - 2\alpha_N)], \\ \text{Sp}_3 &= c_-^4 [2c_+^6 (3 + \alpha_N) + c_+^4 (7 - 5\alpha_N) + c_+^2 (\alpha_N^3 + 9\alpha_N^2 - \alpha_N + 3) + (3 - \alpha_N) \alpha_N^2]. \end{aligned} \quad (31)$$

The comparison between our analytical approximation (28) [with additional next-to-leading order correction (30) for a relatively large $\alpha_N = 0.24, 0.3$] and the exact numerical evaluations is presented in Fig. 2 with perfect match in the nonrelativistic limit. Note that the crossing of curves for relatively large α_N at relatively large ξ_w is due to the nonmonotonous dependence of the wall pressure difference on α_N at relatively large ξ_w . This can be easily illustrated in the case of a simple bag EOS [80] with $c_+ = c_- = 1/\sqrt{3}$, in which case the wall pressure difference $p_+ - p_-$ reads

$$\frac{p_+ - p_-}{w_N} = \frac{w_+ \bar{\gamma}_+^2 \bar{v}_+ (\bar{v}_- - \bar{v}_+),}{w_N} \quad (32)$$

after using the junction conditions $w_- \bar{\gamma}_-^2 \bar{v}_- = w_+ \bar{\gamma}_+^2 \bar{v}_+$ and $w_- \bar{\gamma}_-^2 \bar{v}_-^2 + p_- = w_+ \bar{\gamma}_+^2 \bar{v}_+^2 + p_+$. When the bubble wall velocity ξ_w is small, the fluid profile is deflagration and hence the wall-frame fluid velocity just behind the

wall reads $\bar{v}_- = \xi_w$. For $w_+/w_N = \alpha_N/\alpha_N = 1 + \mathcal{O}(\xi_w)$, we take $w_+/w_N \simeq 1$ and then (32) turns into

$$\frac{p_+ - p_-}{w_N} = \frac{\bar{v}_+}{1 - \bar{v}_+^2} (\xi_w - \bar{v}_+). \quad (33)$$

As one can explicitly check numerically, although the wall-frame fluid velocity just in front of the wall \bar{v}_+ decreases with an increasing α_N , the wall-pressure difference is not a monotonic function of \bar{v}_+ , and hence it is also nonmonotonic to α_N . For example, for a small ξ_w , the leading-order wall pressure difference in the bag case,

$$\frac{\Delta_{\text{wall}} p}{w_N} \Big|_{\text{LO}} = 9 \left(\frac{1}{3} - \alpha_N \right) \alpha_N \xi_w^2, \quad (34)$$

will be larger if α_N is closer to $1/6$. However, when ξ_w is relatively larger, we need take into account the NLO

term,

$$\left. \frac{\Delta_{\text{wall}P}}{w_N} \right|_{\text{NLO}} = 9(\alpha_N - 8\alpha_N^2 + 36\alpha_N^3 - 9\alpha_N^4)\xi_w^4. \quad (35)$$

where the quartic coefficient increases as α_N increases. Therefore, when ξ_w is relatively large, the wall pressure difference of large α_N is larger than that of small α_N .

V. CONCLUSIONS AND DISCUSSIONS

The cosmological FOPT serves as an indispensable probe into the early Universe for the new physics beyond the standard model of particle physics. The weakly coupled FOPT is widely studied for its validity in adopting the perturbative field theory method to estimate the vacuum decay rate and bubble wall velocity. However, this is not the case for the strongly coupled FOPTs where the perturbative method ceases to apply for lack of perturbative definitions on the effective potential and collision terms in Boltzmann equations. Fortunately, the holographic method as a specific realization of the strong-weak duality can map the strongly coupled FOPT on the boundary into a weakly coupled gravity theory in the bulk. Recent holographic numerical simulations of strongly coupled FOPTs not only prefer a nonrelativistic terminal wall velocity but also confirm the perfect-fluid hydrodynamics approximation, and in particular, reveal an intriguing linear correlation between the phase pressure difference and terminal velocity of planar wall. By fully appreciating the perfect-fluid hydrodynamics, we analytically reproduce such a correlation not only for the planar wall but also for cylindrical and spherical walls in the case with a bag EOS. To be more close to the realistic case, we generalize in this paper our previous analytic results into the case with a ν -model EOS beyond the simple bag model. The analytic approximations of the phase pressure difference (16), (20), and (24) we obtained for the planar, cylindrical, and spherical walls, respectively, not only well-match the exact numerical evaluations from the perfect-fluid hydrodynamics, but also improve our previous results in the bag limit $c_{\pm} \rightarrow c_s$,

$$\left(\frac{p_O - p_N}{w_N} \right)_{c_{\pm} \rightarrow c_s}^{D=0} = \frac{\alpha_N}{c_s} \xi_w + \mathcal{O}(\xi_w^2), \quad (36)$$

$$\left(\frac{p_O - p_N}{w_N} \right)_{c_{\pm} \rightarrow c_s}^{D=1} = \left[\frac{\alpha_N^2}{2c_s^4} - \frac{\alpha_N}{c_s^2} \left(1 + \ln \frac{\xi_w}{2c_s} \right) \right] \xi_w^2 + \mathcal{O}(\xi_w^4), \quad (37)$$

$$\left(\frac{p_O - p_N}{w_N} \right)_{c_{\pm} \rightarrow c_s}^{D=2} = \left(\frac{\alpha_N}{c_s^2} + \frac{\alpha_N^2}{2c_s^4} \right) \xi_w^2 + \mathcal{O}(\xi_w^4). \quad (38)$$

All these analytic results can be directly tested in future holographic numerical simulations (see, for example, the last panel of Fig. 3 for a perfect match between our analytic approximation (16) and holographic numerical sim-

ulation [73] in the case with an expanding planar wall), which would shed light on the understanding of strongly coupled FOPT and its holographic dual.

ACKNOWLEDGMENTS

We thank Mikel Sanchez Garitaonandia for helpful correspondence and for providing the original data. We also thank an anonymous referee for insightful suggestions in greatly improving the presentations. S.J.W. is supported by the National Key Research and Development Program of China Grant No. 2021YFC2203004, No. 2020YFC2201501 and No. 2021YFA0718304, the National Natural Science Foundation of China Grants No. 12105344, No. 12235019, and No. 12047503, the Key Research Program of the Chinese Academy of Sciences (CAS) Grant No. XDPB15, the Key Research Program of Frontier Sciences of CAS, and the Science Research Grants from the China Manned Space Project No. CMS-CSST-2021-B01.

Appendix A: Hydrodynamics beyond bag EOS

In this appendix, we revisit in detail the hydrodynamics beyond the bag EOS specifically in the ν -model [85] where the sound velocity profile $c_s(\xi)$ takes constant values c_- and c_+ inside ($\xi < \xi_w$) and outside ($\xi > \xi_w$) of the bubble wall, respectively. This ν -model EOS together with the junction conditions (4) and (5) across the bubble wall gives rise to the hydrodynamic solution (10) which we repeat here at your convenience,

$$\bar{v}_+ = \frac{1}{1 + \alpha_+} \left(qX_+ \pm \sqrt{q^2 X_-^2 + \alpha_+^2 + (1 - c_+^2)\alpha_+ + q^2 c_-^2 - c_+^2} \right). \quad (\text{A1})$$

Here abbreviations $q \equiv (1 + c_+^2)/(1 + c_-^2)$, $X_{\pm} \equiv \bar{v}_-/2 \pm c_-^2/(2\bar{v}_-)$, $\alpha_+ \equiv \Delta V_0/(a_+ T_+^{\nu+})$, and $\Delta V_0 \equiv V_0^+ - V_0^-$ are introduced for clarity. Similar to the bag-EOS case, the detonation (deflagration) mode picks the plus-sign (minus-sign) branch of (A1). Note that in order for \bar{v}_+ in (A1) to be real positive number, α_+ should be bounded from below by $(c_+^2 - c_-^2)/(1 + c_-^2)$, and for $\alpha_+ > c_+^2$, only the detonation mode exists. Note also that the condition $\bar{v}_- = c_-$ defines the Jouguet velocity, which further defines the Jouguet detonation (deflagration) mode when \bar{v}_+ in the plus-sign (minus-sign) branch of (A1) takes its minimal (maximal) value as

$$v_J^{\text{det}}(\alpha_+) = \frac{qc_- + \sqrt{q^2 c_-^2 - (1 + \alpha_+)(c_+^2 - \alpha_+)}}{1 + \alpha_+}, \quad (\text{A2})$$

$$v_J^{\text{def}}(\alpha_+) = \frac{qc_- - \sqrt{q^2 c_-^2 - (1 + \alpha_+)(c_+^2 - \alpha_+)}}{1 + \alpha_+}. \quad (\text{A3})$$

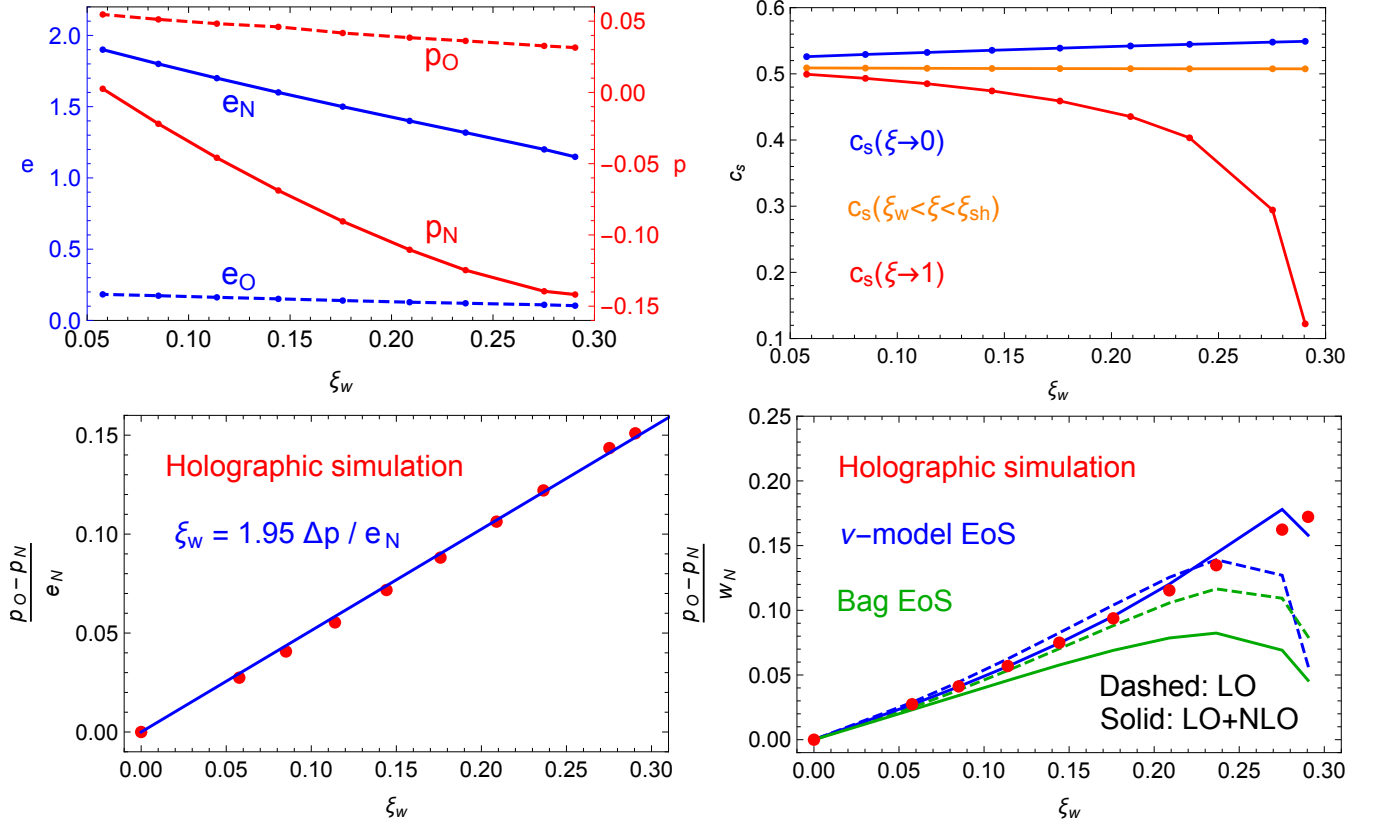


FIG. 3. The original data points from Ref. [73] for the energy density and pressure (first panel) as well as sound velocity (second panel) with respect to the wall velocity. The third panel reproduces their original fit to the phase pressure difference in unit of asymptotic energy density, which is actually achieved highly nontrivial by adjusting the strength factor and EOS simultaneously. The last panel compares the data points from the holographic numerical simulation to our analytic approximation (16) from both bag EOS and ν -model EOS.

It is worth noting that if α_+ takes its minimal value $(c_+^2 - c_-^2)/(1 + c_-^2)$, we have $v_J^{\text{det}}|_{\min} = v_J^{\text{def}}|_{\max} = c_-$, that is to say, we always have $v_J^{\text{det}} \geq c_-$ and $v_J^{\text{def}} \leq c_-$.

After specifying the physical branches of hydrodynamic solutions for different expansion modes, we can solve the fluid velocity profile $v(\xi)$ from the hydrodynamic EoM (2) given corresponding junction conditions (4) and (6) at the bubble wall and shockwave front, if any. We illustrate the fluid velocity profiles $v(\xi)$ naively solved from (2) in Fig. 4 for some particular values of the sound velocity. Note that $(\xi = c_s, v = 0)$ is an improper node of (2), where all of $v(\xi)$ curves are approached from $c_s + 0^+$. The expansion modes are separated by the rarefaction front $\mu(\xi, v) = c_-$ and shockwave front $\mu(\xi, v)\xi = c_+^2$. We next turn to solve the fluid velocity and enthalpy profiles specifically for different expansion modes.

1. Weak detonation

The detonation mode is defined when the fluid velocity in front of the bubble wall is vanished, $v(\xi > \xi_w) = 0$,

namely $\bar{v}_+ = \xi_w$ in the wall frame. Thus, \bar{v}_- can be solved from the plus-sign branch of (A1), leading directly to $v_- = \mu(\xi_w, \bar{v}_-)$. Hence the condition $v_- > v_+ = 0$ namely $\bar{v}_+ > \bar{v}_-$ defines the detonation mode. The detonation mode can be of either weak or Jouguet types with $\bar{v}_- > c_-$ or $\bar{v}_- = c_-$, that is $\xi_w > v_J^{\text{det}}$ or $\xi_w = v_J^{\text{det}}$, respectively. We postpone the discussion of the Jouguet detonation until Sec. A 4, but first solve here the hydrodynamic EoM (2) with $c_s = c_-$ for the fluid velocity profile $v(\xi)$ passing through (ξ_w, v_-) in the case of weak detonation ($\xi_w > v_J^{\text{det}}$) as illustrated in the left panel of Fig. 5. Note that for the ν -model EOS, the weak detonation mode contains not only the case with a large $\xi_w > v_J^{\text{det}} > c_+$ but also the case with a very large $\xi_w > c_+^2/v_J^{\text{det}} > v_J^{\text{det}}$. As a comparison for a bag EOS with $c_+ = c_- = c_s$, only the former case $\xi_w > v_J^{\text{det}} > c_s$ survives. With the fluid velocity profile $v(\xi)$ solved from (2) at hand, the corresponding enthalpy profile $w(\xi)$ can be obtained simply by integrating (3) from the point (ξ_w, w_-) with the enthalpy w_- just behind the wall determined by the junction condition (4) from the enthalpy $w_+ = w_N$ in front of the wall up to the null infinity. We illustrate the enthalpy profile for the

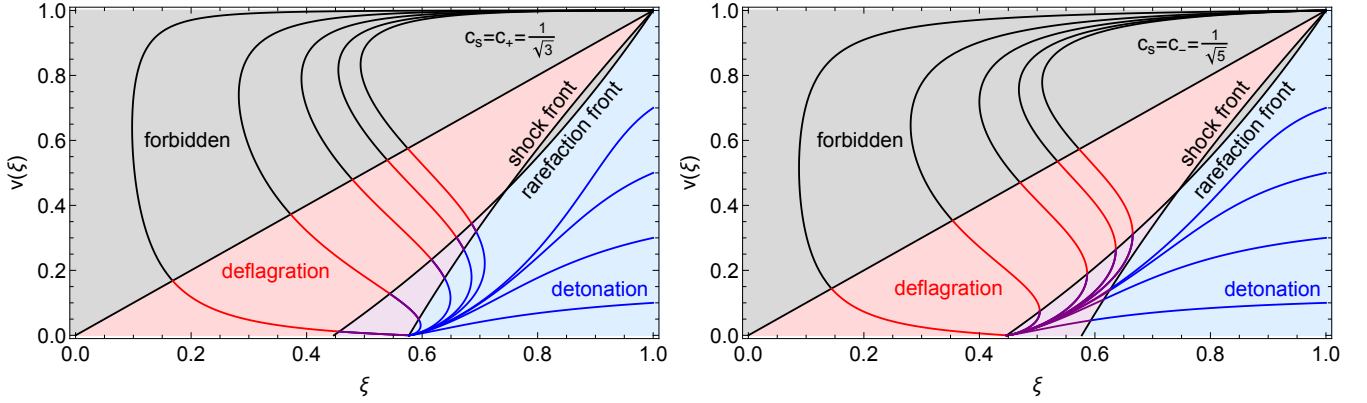


FIG. 4. The fluid velocity profiles $v(\xi)$ for a ν -model EOS with $c_s = c_+ = 1/\sqrt{3}$ (left) and $c_s = c_- = 1/\sqrt{5}$ (right). The shockwave front is defined by $\mu(\xi, v)\xi = c_+^2$ while the rarefaction front is defined by $\mu(\xi, v) = c_-$. The gray, red, blue, and purple shaded regions correspond to the forbidden, deflagration, detonation, hybrid profiles, respectively.

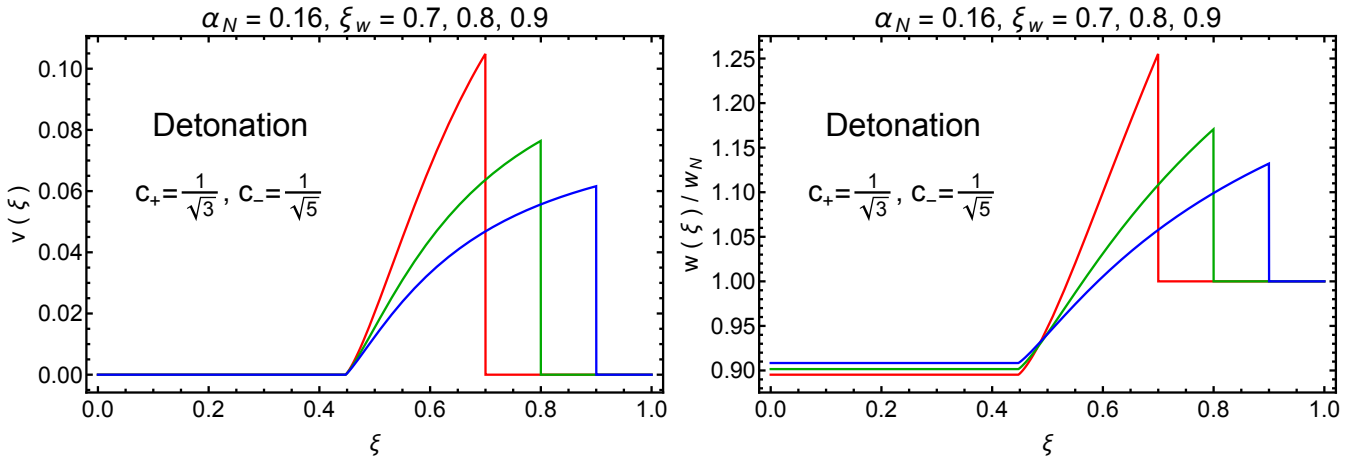


FIG. 5. The profiles of the fluid velocity $v(\xi)$ (left) and enthalpy $w(\xi)/w_N$ (right) for the weak detonation mode. We fix $\alpha_N = 0.16$ and take $c_+ = 1/\sqrt{3}$, $c_- = 1/\sqrt{5}$ for illustration. The red, green, and blue curves correspond to the bubble wall velocities $\xi_w = 0.7, 0.8, 0.9$, respectively.

weak detonation in the right panel of Fig. 5.

2. Weak deflagration

The deflagration mode is defined when the fluid velocity behind the bubble wall is vanished, $v(\xi < \xi_w) = 0$, namely $\bar{v}_- = \xi_w$ in the wall frame. Thus, \bar{v}_+ can be solved from the minus-sign branch of (A1), leading directly to $v_+ = \mu(\xi_w, \bar{v}_+)$. Hence the condition $v_+ > v_- = 0$ namely $\bar{v}_- > \bar{v}_+$ defines the deflagration mode. The deflagration mode can be of either weak or Jouguet types with $\xi_w = \bar{v}_- < c_-$ or $\xi_w = \bar{v}_- = c_-$, that is $\xi_w < v_J^{\text{def}}$ or $\xi_w = v_J^{\text{def}}$, respectively. We postpone the discussion of the Jouguet deflagration until Sec. A 3, but first solve here the hydrodynamic EoM (2) with $c_s = c_-$ for the fluid velocity profile $v(\xi)$ passing through (ξ_w, v_+) in the case of weak deflagration ($\xi_w < v_J^{\text{def}}$) as illustrated in the left panel of Fig. 6. Note that the

solved fluid velocity profile $v(\xi)$ should be cut off due to the shockwave front at ξ_{sh} with corresponding fluid velocity $v_{sh} \equiv v(\xi_{sh} + 0^-)$, both of which can be determined as shown shortly below. First, it is easy to find $\tilde{v}_L \tilde{v}_R = c_+^2$ for the shock-frame fluid velocities $\tilde{v}_{L/R}$ just inside/outside of the shockwave front since the whole shockwave is in the symmetric phase in front of the bubble wall. Then, as the fluid velocity in front of the shockwave front is at rest, $v_R = \mu(\xi_{sh}, \tilde{v}_R) = 0$, the shockwave front velocity $\xi_{sh} = \tilde{v}_R = c_+^2 / \tilde{v}_L = c_+^2 / \mu(\xi_{sh}, v_L)$ can be directly solved from $v_L = v(\xi_{sh} + 0^-) \equiv v_{sh}$ given by extrapolating the solved profile of $v(\xi)$ from (ξ_w, v_+) to (ξ_{sh}, v_{sh}) . The enthalpy profile $w(\xi)$ shown in the right panel of Fig. 6 can be obtained by integrating the fluid EoM (3) from the shock front (ξ_{sh}, w_L) all the way back to the wall, where $w_L \equiv w(\xi_{sh} + 0^-)$ can be determined by the junction condition (6) with $w_R = w_N$, $\tilde{v}_R = \xi_{sh}$, and $\tilde{v}_L = \mu(\xi_{sh}, v_{sh})$. At the bubble wall, the enthalpy profile experiences a sudden jump from $w_+ = w(\xi_w + 0^+)$ to w_-

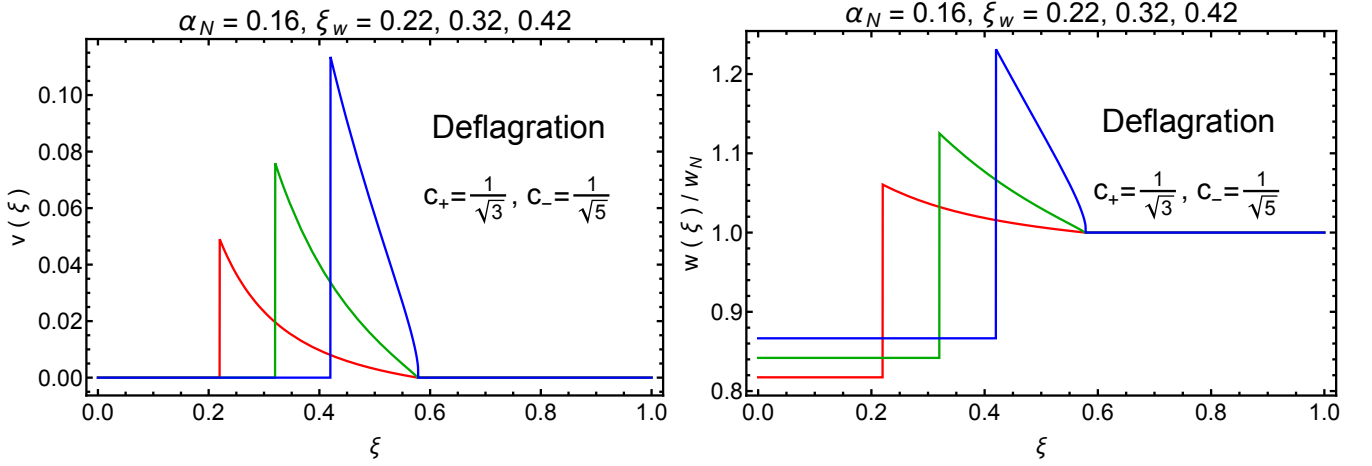


FIG. 6. The fluid profiles $v(\xi)$ (left) and $w(\xi)/w_N$ (right) of the weak deflagration mode. We fix $\alpha_N = 0.16$ and take $c_+ = 1/\sqrt{3}$, $c_- = 1/\sqrt{5}$. The red, green, and blue lines correspond to the bubble wall velocity ξ_w takes the value of 0.22, 0.32 and 0.42, respectively.

determined by the junction condition (4) with $\bar{v}_- = \xi_w$ and $\bar{v}_+(\alpha_+, \xi_w)$ given by the minus-sign branch of (10).

3. Jouguet deflagration

The Jouguet deflagration mode (or we call it the hybrid mode in the bag model) is a special deflagration mode ($\bar{v}_+ < \bar{v}_-$) of Jouguet type ($\bar{v}_- = c_-$) corresponding to the minus-sign branch of (10) and realized with the wall velocity lying between $c_- < \xi_w < v_J^{\text{det}}$. The fluid velocity profile in Fig. 7 contains both compressive shockwave and rarefaction wave in the front and back of the bubble wall, respectively, as derived shortly below. The Jouguet deflagration condition $\bar{v}_- = c_-$ leads to $\bar{v}_+ = v_J^{\text{def}}$ from (A3) by (10), giving rise to $v(\xi_w + 0^+) \equiv v_+ = \mu(\xi_w, v_J^{\text{def}})$ and $v(\xi_w + 0^-) \equiv v_- = \mu(\xi_w, c_-)$ that can be used to solve the fluid EoM (2) both forward and backward from $(\xi_w + 0^+, v_+)$ and $(\xi_w + 0^-, v_-)$ with $c_s = c_+$ and $c_s = c_-$, respectively. The solved velocity profile again vanishes in front of the shockwave front $\xi = \xi_{sh} + 0^+$ and behind $\xi = c_- + 0^-$ as in the weak deflagration and weak detonation cases. The enthalpy profile can be similarly obtained from integrating (3) backward from both $w(\xi_{sh} + 0^-) = w_L$ and $w(\xi_w + 0^-) = w_-$, where the enthalpies w_L and w_- are sequentially determined by the junction conditions (6) and (4) with $w_R = w_N$, $\tilde{v}_R = \xi_{sh}$, $\tilde{v}_L = \mu(\xi_{sh}, v_{sh})$ and $w_+ = w(\xi_w + 0^+)$, $\bar{v}_+ = v_J^{\text{def}}$, $\bar{v}_- = c_-$, respectively.

4. Jouguet detonation

The Jouguet detonation mode (absent in the bag model) is a special detonation mode ($\bar{v}_+ > \bar{v}_-$) of Jouguet type ($\bar{v}_- = c_-$) corresponding to the plus-sign branch of (10) realized by $\bar{v}_+ = v_J^{\text{det}}(\alpha_+)$. Sim-

ilar to the Jouguet deflagration mode, the fluid velocity profile of Jouguet detonation mode in Fig. 8 also contains both compressive shockwave and rarefaction wave in the front and back of the bubble wall, respectively, but corresponding to the purple region in Fig. 4. To derive the fluid velocity profile, the Jouguet detonation condition $\bar{v}_- = c_-$ leads to $\bar{v}_+ = v_J^{\text{det}}$ from (A2) by (10), giving rise to $v(\xi_w + 0^-) \equiv v_+ = \mu(\xi_w, c_-)$ and $v(\xi_w + 0^+) \equiv v_- = \mu(\xi_w, v_J^{\text{det}})$ that can be used to solve the fluid EoM (2) both forward and backward from $(\xi_w + 0^+, v_+)$ and $(\xi_w + 0^-, v_-)$ with $c_s = c_+$ and $c_s = c_-$, respectively. The solved velocity profile again vanishes in front of the shockwave front $\xi = \xi_{sh} + 0^+$ and behind $\xi = c_- + 0^-$ as in the weak deflagration and weak detonation cases. The enthalpy profile can be similarly obtained from integrating (3) backward from both $w(\xi_{sh} + 0^-) = w_L$ and $w(\xi_w + 0^-) = w_-$, where the enthalpies w_L and w_- are sequentially determined by the junction conditions (6) and (4) with $w_R = w_N$, $\tilde{v}_R = \xi_{sh}$, $\tilde{v}_L = \mu(\xi_{sh}, v_{sh})$ and $w_+ = w(\xi_w + 0^+)$, $\bar{v}_+ = v_J^{\text{det}}$, $\bar{v}_- = c_-$, respectively.

Finally, we discuss the condition where the Jouguet detonation mode can be realized. The difference between the weak detonation and Jouguet detonation mode is that the Jouguet detonation mode has a compressive shockwave in front of the wall. From the analysis of the weak deflagration mode, we can figure out that the situation where a shockfront can exist is $\mu(\xi_{sh}, v_{sh})\xi_{sh} < c_+^2$, corresponding to the red and purple regions in Fig. 4. If the condition cannot be satisfied even at $\xi_{sh} = \xi_w$, the compressive shockwave must vanish and only weak detonation mode exists. Since just right in front of the wall $\mu(\xi_w, v_+)$ takes the value of v_J^{det} , we can derive that the form of the condition $\mu(\xi_{sh}, v_{sh})\xi_{sh} < c_+^2$ turns into $v_J^{\text{det}}\xi_w < c_+^2$ at $\xi_{sh} = \xi_w$, leading to $\xi_w < c_+^2/v_J^{\text{det}}$. Recall that for a detonation mode $\bar{v}_- < \bar{v}_+ < \xi_w$, we must have $\xi_w > \bar{v}_+|_{\min} = v_J^{\text{det}}$. Hence, the existence of both detona-

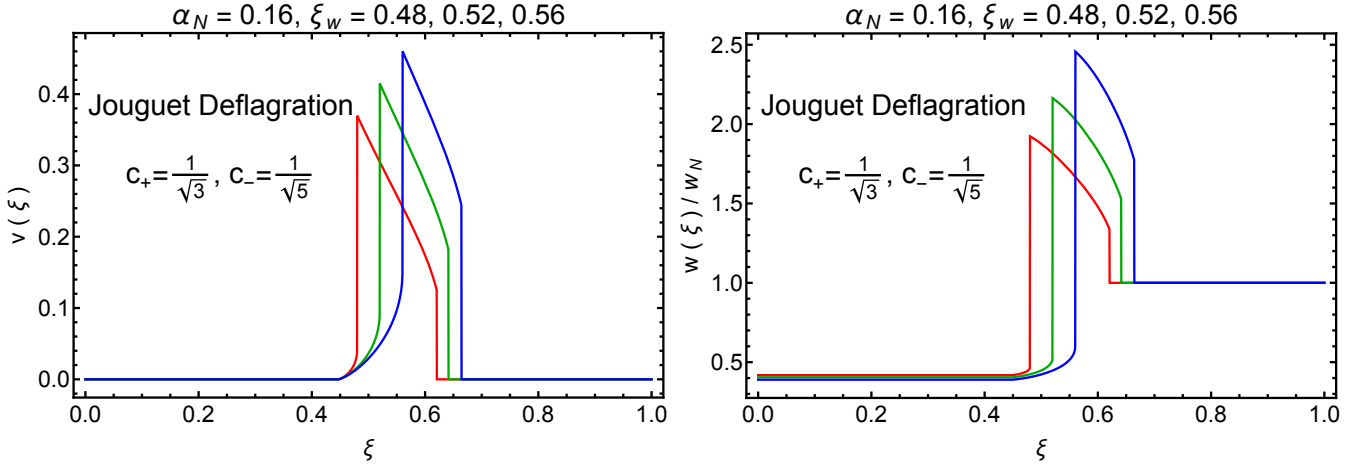


FIG. 7. The fluid profiles $v(\xi)$ (left) and $w(\xi)/w_N$ (right) of the Jouguet deflagration mode. We fix $\alpha_N = 0.16$ and take $c_+ = 1/\sqrt{3}$, $c_- = 1/\sqrt{5}$. The red, green and blue lines correspond to the bubble wall velocity ξ_w taking the value of 0.48, 0.52, and 0.56, respectively.

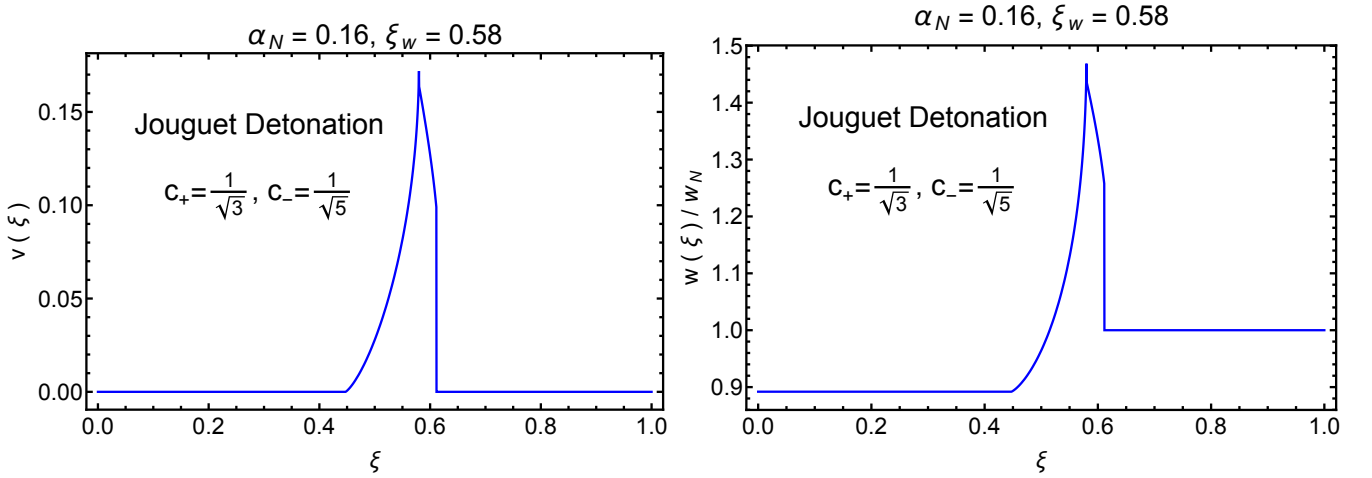


FIG. 8. The fluid profiles $v(\xi)$ (left) and $w(\xi)/w_N$ (right) of the Jouguet detonation mode. We fix $\alpha_N = 0.16$ and take $c_+ = 1/\sqrt{3}$, $c_- = 1/\sqrt{5}$. The blue lines correspond to the bubble wall velocity ξ_w taking the value of 0.58.

tion profile as well as the shockwave can only be realized when $v_J^{\text{det}} < \xi_w < c_+^2/v_J^{\text{det}}$, that is exactly the condition where the Jouguet detonation mode can be realized. Note that if $c_+ < v_J^{\text{det}}$, the condition $v_J^{\text{det}} < \xi_w < c_+^2/v_J^{\text{det}}$ cannot be satisfied at all. Therefore, the condition of the realization of the Jouguet detonation can be concluded

as

$$v_J^{\text{det}} < \xi_w < \frac{c_+^2}{v_J^{\text{det}}}, \quad \text{if } c_+ > v_J^{\text{det}} \quad (\text{A4})$$

no Jouguet detonation mode, if $c_+ < v_J^{\text{det}}$.

Recall that we have shown the minimum of $v_J^{\text{det}}(\alpha_+)$ is c_- , then when $c_+ < c_-$, the condition $c_+ > v_J^{\text{det}}$ cannot be satisfied at all and the purple region will vanish in Fig. 4. Therefore, the Jouguet detonation mode can exist only in the $c_+ > c_-$ case.

[1] Anupam Mazumdar and Graham White, “Review of cosmic phase transitions: their significance and experimental signatures,” Rept. Prog. Phys. **82**, 076901 (2019),

arXiv:1811.01948 [hep-ph].

[2] Mark B. Hindmarsh, Marvin Lüben, Johannes Lumma, and Martin Pauly, “Phase transitions in the early

- universe,” *SciPost Phys. Lect. Notes* **24**, 1 (2021), arXiv:2008.09136 [astro-ph.CO].
- [3] Mariano Quiros, “Finite temperature field theory and phase transitions,” in *ICTP Summer School in High-Energy Physics and Cosmology* (1999) pp. 187–259, arXiv:hep-ph/9901312.
- [4] Peter Athron, Csaba Balázs, Andrew Fowlie, Lachlan Morris, and Lei Wu, “Cosmological phase transitions: from perturbative particle physics to gravitational waves,” (2023), arXiv:2305.02357 [hep-ph].
- [5] Rong-Gen Cai and Shao-Jiang Wang, “Effective picture of bubble expansion,” *JCAP* **2021**, 096 (2021), arXiv:2011.11451 [astro-ph.CO].
- [6] Marek Lewicki and Ville Vaskonen, “Gravitational waves from bubble collisions and fluid motion in strongly supercooled phase transitions,” *Eur. Phys. J. C* **83**, 109 (2023), arXiv:2208.11697 [astro-ph.CO].
- [7] Shao-Jiang Wang and Zi-Yan Yuwen, “Hydrodynamic backreaction force of cosmological bubble expansion,” *Phys. Rev. D* **107**, 023501 (2023), arXiv:2205.02492 [hep-ph].
- [8] Jun-Chen Wang, Zi-Yan Yuwen, Yu-Shi Hao, and Shao-Jiang Wang, “General backreaction force of cosmological bubble expansion,” (2023), arXiv:2310.07691 [hep-ph].
- [9] Ryusuke Jinno and Masahiro Takimoto, “Gravitational waves from bubble collisions: An analytic derivation,” *Phys. Rev.* **D95**, 024009 (2017), arXiv:1605.01403 [astro-ph.CO].
- [10] Ryusuke Jinno and Masahiro Takimoto, “Gravitational waves from bubble dynamics: Beyond the Envelope,” *JCAP* **1901**, 060 (2019), arXiv:1707.03111 [hep-ph].
- [11] Thomas Konstandin, “Gravitational radiation from a bulk flow model,” *JCAP* **1803**, 047 (2018), arXiv:1712.06869 [astro-ph.CO].
- [12] Haowen Zhong, Biping Gong, and Taotao Qiu, “Gravitational waves from bubble collisions in FLRW spacetime,” *JHEP* **02**, 77 (2022), arXiv:2107.01845 [gr-qc].
- [13] Mark Hindmarsh, Stephan J. Huber, Kari Rummukainen, and David J. Weir, “Gravitational waves from the sound of a first order phase transition,” *Phys. Rev. Lett.* **112**, 041301 (2014), arXiv:1304.2433 [hep-ph].
- [14] Mark Hindmarsh, Stephan J. Huber, Kari Rummukainen, and David J. Weir, “Numerical simulations of acoustically generated gravitational waves at a first order phase transition,” *Phys. Rev.* **D92**, 123009 (2015), arXiv:1504.03291 [astro-ph.CO].
- [15] Mark Hindmarsh, Stephan J. Huber, Kari Rummukainen, and David J. Weir, “Shape of the acoustic gravitational wave power spectrum from a first order phase transition,” *Phys. Rev.* **D96**, 103520 (2017), [erratum: *Phys. Rev.D101,no.8,089902(2020)*], arXiv:1704.05871 [astro-ph.CO].
- [16] Mark Hindmarsh, “Sound shell model for acoustic gravitational wave production at a first-order phase transition in the early Universe,” *Phys. Rev. Lett.* **120**, 071301 (2018), arXiv:1608.04735 [astro-ph.CO].
- [17] Mark Hindmarsh and Mulham Hijazi, “Gravitational waves from first order cosmological phase transitions in the Sound Shell Model,” *JCAP* **1912**, 062 (2019), arXiv:1909.10040 [astro-ph.CO].
- [18] Huai-Ke Guo, Kuver Sinha, Daniel Vagie, and Graham White, “Phase Transitions in an Expanding Universe: Stochastic Gravitational Waves in Standard and Non-Standard Histories,” *JCAP* **01**, 001 (2021), arXiv:2007.08537 [hep-ph].
- [19] Rong-Gen Cai, Shao-Jiang Wang, and Zi-Yan Yuwen, “Hydrodynamic sound shell model,” *Phys. Rev. D* **108**, L021502 (2023), arXiv:2305.00074 [gr-qc].
- [20] Ramkishor Sharma, Jani Dahl, Axel Brandenburg, and Mark Hindmarsh, “Shallow relic gravitational wave spectrum with acoustic peak,” (2023), arXiv:2308.12916 [gr-qc].
- [21] Alberto Roper Pol, Simona Procacci, and Chiara Caprini, “Characterization of the gravitational wave spectrum from sound waves within the sound shell model,” (2023), arXiv:2308.12943 [gr-qc].
- [22] Chiara Caprini et al., “Science with the space-based interferometer eLISA. II: Gravitational waves from cosmological phase transitions,” *JCAP* **1604**, 001 (2016), arXiv:1512.06239 [astro-ph.CO].
- [23] Chiara Caprini et al., “Detecting gravitational waves from cosmological phase transitions with LISA: an update,” *JCAP* **2003**, 024 (2020), arXiv:1910.13125 [astro-ph.CO].
- [24] Jing Liu, Ligong Bian, Rong-Gen Cai, Zong-Kuan Guo, and Shao-Jiang Wang, “Constraining First-Order Phase Transitions with Curvature Perturbations,” *Phys. Rev. Lett.* **130**, 051001 (2023), arXiv:2208.14086 [astro-ph.CO].
- [25] Jing Liu, Ligong Bian, Rong-Gen Cai, Zong-Kuan Guo, and Shao-Jiang Wang, “Primordial black hole production during first-order phase transitions,” *Phys. Rev. D* **105**, L021303 (2022), arXiv:2106.05637 [astro-ph.CO].
- [26] Katsuya Hashino, Shinya Kanemura, and Tomo Takahashi, “Primordial black holes as a probe of strongly first-order electroweak phase transition,” (2021), arXiv:2111.13099 [hep-ph].
- [27] Song He, Li Li, Zhibin Li, and Shao-Jiang Wang, “Gravitational Waves and Primordial Black Hole Productions from Gluodynamics,” (2022), arXiv:2210.14094 [hep-ph].
- [28] Marek Lewicki, Piotr Toczek, and Ville Vaskonen, “Primordial black holes from strong first-order phase transitions,” *JHEP* **09**, 092 (2023), arXiv:2305.04924 [astro-ph.CO].
- [29] Yann Gouttenoire and Tomer Volansky, “Primordial Black Holes from Supercooled Phase Transitions,” (2023), arXiv:2305.04942 [hep-ph].
- [30] Jason Baldes and María Olalla Olea-Romacho, “Primordial black holes as dark matter: Interferometric tests of phase transition origin,” (2023), arXiv:2307.11639 [hep-ph].
- [31] Rong-Gen Cai, Zhoujian Cao, Zong-Kuan Guo, Shao-Jiang Wang, and Tao Yang, “The Gravitational-Wave Physics,” *Natl. Sci. Rev.* **4**, 687–706 (2017), arXiv:1703.00187 [gr-qc].
- [32] Ligong Bian et al., “The Gravitational-wave physics II: Progress,” *Sci. China Phys. Mech. Astron.* **64**, 120401 (2021), arXiv:2106.10235 [gr-qc].
- [33] Robert Caldwell et al., “Detection of early-universe gravitational-wave signatures and fundamental physics,” *Gen. Rel. Grav.* **54**, 156 (2022), arXiv:2203.07972 [gr-qc].
- [34] Rong-Gen Cai, Katsuya Hashino, Shao-Jiang Wang, and Jiang-Hao Yu, “Gravitational waves from patterns of electroweak symmetry breaking: an effective perspective,” (2022), arXiv:2202.08295 [hep-ph].
- [35] Wang-Wei Yu and Shao-Jiang Wang, “Searching for double-peak and doubly broken gravitational-wave spectra from Advanced LIGO-Virgo’s first three ob-

- serving runs,” *Phys. Rev. D* **108**, 063526 (2023), arXiv:2211.13111 [gr-qc].
- [36] Alba Romero, Katarina Martinovic, Thomas A. Callister, Huai-Ke Guo, Mario Martínez, Mairi Sakellariadou, Feng-Wei Yang, and Yue Zhao, “Implications for First-Order Cosmological Phase Transitions from the Third LIGO-Virgo Observing Run,” *Phys. Rev. Lett.* **126**, 151301 (2021), arXiv:2102.01714 [hep-ph].
- [37] Fei Huang, Veronica Sanz, Jing Shu, and Xiao Xue, “LIGO as a probe of dark sectors,” *Phys. Rev. D* **104**, 095001 (2021), arXiv:2102.03155 [hep-ph].
- [38] Yang Jiang and Qing-Guo Huang, “Constraining the gravitational-wave spectrum from cosmological first-order phase transitions using data from LIGO-Virgo first three observing runs,” *JCAP* **06**, 053 (2023), arXiv:2203.11781 [astro-ph.CO].
- [39] Charles Badger *et al.*, “Probing early Universe supercooled phase transitions with gravitational wave data,” *Phys. Rev. D* **107**, 023511 (2023), arXiv:2209.14707 [hep-ph].
- [40] Heng Xu *et al.*, “Searching for the Nano-Hertz Stochastic Gravitational Wave Background with the Chinese Pulsar Timing Array Data Release I,” *Res. Astron. Astrophys.* **23**, 075024 (2023), arXiv:2306.16216 [astro-ph.HE].
- [41] Gabriella Agazie *et al.* (NANOGrav), “The NANOGrav 15 yr Data Set: Evidence for a Gravitational-wave Background,” *Astrophys. J. Lett.* **951**, L8 (2023), arXiv:2306.16213 [astro-ph.HE].
- [42] J. Antoniadis *et al.* (EPTA), “The second data release from the European Pulsar Timing Array I. The dataset and timing analysis,” *Astron. Astrophys.* **678**, A48 (2023), arXiv:2306.16224 [astro-ph.HE].
- [43] Daniel J. Reardon *et al.*, “Search for an Isotropic Gravitational-wave Background with the Parkes Pulsar Timing Array,” *Astrophys. J. Lett.* **951**, L6 (2023), arXiv:2306.16215 [astro-ph.HE].
- [44] Adeela Afzal *et al.* (NANOGrav), “The NANOGrav 15 yr Data Set: Search for Signals from New Physics,” *Astrophys. J. Lett.* **951**, L11 (2023), arXiv:2306.16219 [astro-ph.HE].
- [45] Andrea Addazi, Yi-Fu Cai, Antonino Marciano, and Luca Visinelli, “Have pulsar timing array methods detected a cosmological phase transition?” (2023), arXiv:2306.17205 [astro-ph.CO].
- [46] Peter Athron, Andrew Fowlie, Chih-Ting Lu, Lachlan Morris, Lei Wu, Yongcheng Wu, and Zhongxiu Xu, “Can supercooled phase transitions explain the gravitational wave background observed by pulsar timing arrays?” (2023), arXiv:2306.17239 [hep-ph].
- [47] Kohei Fujikura, Sudhakantha Girmohanta, Yuichiro Nakai, and Motoo Suzuki, “NANOGrav signal from a dark conformal phase transition,” *Phys. Lett. B* **846**, 138203 (2023), arXiv:2306.17086 [hep-ph].
- [48] Chengcheng Han, Ke-Pan Xie, Jin Min Yang, and Mengchao Zhang, “Self-interacting dark matter implied by nano-Hertz gravitational waves,” (2023), arXiv:2306.16966 [hep-ph].
- [49] Gabriele Franciolini, Davide Racco, and Fabrizio Rompineve, “Footprints of the QCD Crossover on Cosmological Gravitational Waves at Pulsar Timing Arrays,” (2023), arXiv:2306.17136 [astro-ph.CO].
- [50] Ligong Bian, Shuailiang Ge, Jing Shu, Bo Wang, Xing-Yu Yang, and Junchao Zong, “Gravitational wave sources for Pulsar Timing Arrays,” (2023), arXiv:2307.02376 [astro-ph.HE].
- [51] Siyu Jiang, Aidi Yang, Jiucheng Ma, and Fa Peng Huang, “Implication of nano-Hertz stochastic gravitational wave on dynamical dark matter through a first-order phase transition,” (2023), arXiv:2306.17827 [hep-ph].
- [52] Tathagata Ghosh, Anish Ghoshal, Huai-Ke Guo, Fazlollah Hajkarim, Stephen F. King, Kuver Sinha, Xin Wang, and Graham White, “Did we hear the sound of the Universe boiling? Analysis using the full fluid velocity profiles and NANOGrav 15-year data,” (2023), arXiv:2307.02259 [astro-ph.HE].
- [53] Yang Xiao, Jin Min Yang, and Yang Zhang, “Implications of Nano-Hertz Gravitational Waves on Electroweak Phase Transition in the Singlet Dark Matter Model,” (2023), arXiv:2307.01072 [hep-ph].
- [54] Shao-Ping Li and Ke-Pan Xie, “Collider test of nano-Hertz gravitational waves from pulsar timing arrays,” *Phys. Rev. D* **108**, 055018 (2023), arXiv:2307.01086 [hep-ph].
- [55] Pasquale Di Bari and Moinul Hossain Rahat, “The split majoron model confronts the NANOGrav signal,” (2023), arXiv:2307.03184 [hep-ph].
- [56] Juan S. Cruz, Florian Niedermann, and Martin S. Sloth, “NANOGrav meets Hot New Early Dark Energy and the origin of neutrino mass,” *Phys. Lett. B* **846**, 138202 (2023), arXiv:2307.03091 [astro-ph.CO].
- [57] Yu-Mei Wu, Zu-Cheng Chen, and Qing-Guo Huang, “Cosmological Interpretation for the Stochastic Signal in Pulsar Timing Arrays,” (2023), arXiv:2307.03141 [astro-ph.CO].
- [58] Xiao Kang Du, Ming Xia Huang, Fei Wang, and Ying Kai Zhang, “Did the nHZ Gravitational Waves Signatures Observed By NANOGrav Indicate Multiple Sector SUSY Breaking?” (2023), arXiv:2307.02938 [hep-ph].
- [59] Yann Gouttenoire, “First-Order Phase Transition Interpretation of Pulsar Timing Array Signal Is Consistent with Solar-Mass Black Holes,” *Phys. Rev. Lett.* **131**, 171404 (2023), arXiv:2307.04239 [hep-ph].
- [60] Moslem Ahmadvand, Ligong Bian, and Soroush Shakeri, “A Heavy QCD Axion model in Light of Pulsar Timing Arrays,” (2023), arXiv:2307.12385 [hep-ph].
- [61] Deng Wang, “Constraining Cosmological Phase Transitions with Chinese Pulsar Timing Array Data Release 1,” (2023), arXiv:2307.15970 [astro-ph.CO].
- [62] Song He, Li Li, Sai Wang, and Shao-Jiang Wang, “Constraints on holographic QCD phase transitions from PTA observations,” (2023), arXiv:2308.07257 [hep-ph].
- [63] Juan Martin Maldacena, “The Large N limit of superconformal field theories and supergravity,” *Adv. Theor. Math. Phys.* **2**, 231–252 (1998), arXiv:hep-th/9711200.
- [64] Edward Witten, “Anti-de Sitter space and holography,” *Adv. Theor. Math. Phys.* **2**, 253–291 (1998), arXiv:hep-th/9802150.
- [65] S. S. Gubser, Igor R. Klebanov, and Alexander M. Polyakov, “Gauge theory correlators from noncritical string theory,” *Phys. Lett. B* **428**, 105–114 (1998), arXiv:hep-th/9802109.
- [66] Francesco Bigazzi, Alessio Caddeo, Aldo L. Cotrone, and Angel Paredes, “Dark Holograms and Gravitational Waves,” *JHEP* **04**, 094 (2021), arXiv:2011.08757 [hep-ph].
- [67] Fëanor Reuben Ares, Mark Hindmarsh, Carlos Hoyos, and Niko Jokela, “Gravitational waves from a holo-

- graphic phase transition,” JHEP **21**, 100 (2020), arXiv:2011.12878 [hep-th].
- [68] Francesco Bigazzi, Alessio Caddeo, Aldo L. Cotrone, and Angel Paredes, “Fate of false vacua in holographic first-order phase transitions,” JHEP **12**, 200 (2020), arXiv:2008.02579 [hep-th].
- [69] Zhou-Run Zhu, Jun Chen, and Defu Hou, “Gravitational waves from holographic QCD phase transition with gluon condensate,” Eur. Phys. J. A **58**, 104 (2022), arXiv:2109.09933 [hep-ph].
- [70] Fëanor Reuben Ares, Oscar Henriksson, Mark Hindmarsh, Carlos Hoyos, and Niko Jokela, “Effective actions and bubble nucleation from holography,” Phys. Rev. D **105**, 066020 (2022), arXiv:2109.13784 [hep-th].
- [71] Fëanor Reuben Ares, Oscar Henriksson, Mark Hindmarsh, Carlos Hoyos, and Niko Jokela, “Gravitational Waves at Strong Coupling from an Effective Action,” Phys. Rev. Lett. **128**, 131101 (2022), arXiv:2110.14442 [hep-th].
- [72] Enrico Morgante, Nicklas Ramberg, and Pedro Schwaller, “Gravitational waves from dark SU(3) Yang-Mills theory,” Phys. Rev. D **107**, 036010 (2023), arXiv:2210.11821 [hep-ph].
- [73] Yago Bea, Jorge Casalderrey-Solana, Thanasis Giannakopoulos, David Mateos, Mikel Sanchez-Garitaonandia, and Miguel Zilhão, “Bubble wall velocity from holography,” Phys. Rev. D **104**, L121903 (2021), arXiv:2104.05708 [hep-th].
- [74] Francesco Bigazzi, Alessio Caddeo, Tommaso Canneti, and Aldo L. Cotrone, “Bubble wall velocity at strong coupling,” JHEP **08**, 090 (2021), arXiv:2104.12817 [hep-ph].
- [75] Romuald A. Janik, Matti Jarvinen, Hesam Soltanpanahi, and Jacob Sonnenschein, “Perfect Fluid Hydrodynamic Picture of Domain Wall Velocities at Strong Coupling,” Phys. Rev. Lett. **129**, 081601 (2022), arXiv:2205.06274 [hep-th].
- [76] Yago Bea, Jorge Casalderrey-Solana, Thanasis Giannakopoulos, Aron Jansen, David Mateos, Mikel Sanchez-Garitaonandia, and Miguel Zilhão, “Holographic bubbles with Jecco: expanding, collapsing and critical,” JHEP **09**, 008 (2022), arXiv:2202.10503 [hep-th].
- [77] Rong-Gen Cai, Song He, Li Li, and Yuan-Xu Wang, “Probing QCD critical point and induced gravitational wave by black hole physics,” Phys. Rev. D **106**, L121902 (2022), arXiv:2201.02004 [hep-th].
- [78] Yan-Qing Zhao, Song He, Defu Hou, Li Li, and Zhibin Li, “Phase diagram of holographic thermal dense QCD matter with rotation,” JHEP **04**, 115 (2023), arXiv:2212.14662 [hep-ph].
- [79] Zhibin Li, Jingmin Liang, Song He, and Li Li, “Holographic study of higher-order baryon number susceptibilities at finite temperature and density,” Phys. Rev. D **108**, 046008 (2023), arXiv:2305.13874 [hep-ph].
- [80] Li Li, Shao-Jiang Wang, and Zi-Yan Yuwen, “Bubble expansion at strong coupling,” Phys. Rev. D **108**, 096033 (2023), arXiv:2302.10042 [hep-th].
- [81] Jose R. Espinosa, Thomas Konstandin, Jose M. No, and Geraldine Servant, “Energy Budget of Cosmological First-order Phase Transitions,” JCAP **1006**, 028 (2010), arXiv:1004.4187 [hep-ph].
- [82] Leonardo Leitaó and Ariel Megevand, “Spherical and non-spherical bubbles in cosmological phase transitions,” Nucl. Phys. B **844**, 450–470 (2011), arXiv:1010.2134 [astro-ph.CO].
- [83] Shao-Jiang Wang and Zi-Yan Yuwen, “The energy budget of cosmological first-order phase transitions beyond the bag equation of state,” JCAP **10**, 047 (2022), arXiv:2206.01148 [hep-ph].
- [84] A. Chodos, R. L. Jaffe, K. Johnson, Charles B. Thorn, and V. F. Weisskopf, “A New Extended Model of Hadrons,” Phys. Rev. D **9**, 3471–3495 (1974).
- [85] Leonardo Leitaó and Ariel Megevand, “Hydrodynamics of phase transition fronts and the speed of sound in the plasma,” Nucl. Phys. **B891**, 159–199 (2015), arXiv:1410.3875 [hep-ph].